

Silicon Nitride Metalenses for Close-to-One Numerical Aperture and Wide-Angle Visible Imaging

Zhi-Bin Fan,^{1,2} Zeng-Kai Shao,^{1,3} Ming-Yuan Xie,^{1,2} Xiao-Ning Pang,^{1,2} Wen-Sheng Ruan,^{1,2} Fu-Li Zhao,^{1,2} Yu-Jie Chen,^{1,3,*} Si-Yuan Yu,^{1,3,4} and Jian-Wen Dong^{1,2,†}

¹*State Key Laboratory of Optoelectronic Materials and Technologies, Sun Yat-sen University, Guangzhou 510275, China*

²*School of Physics, Sun Yat-sen University, Guangzhou 510275, China*

³*School of Electronics and Information Technology, Sun Yat-sen University, Guangzhou 510275, China*

⁴*Photonics Group, Merchant Venturers School of Engineering, University of Bristol, Bristol BS8 1UB, United Kingdom*

(Received 5 February 2018; revised manuscript received 11 May 2018; published 10 July 2018)

Silicon nitride (SiN) is one of the emerging semiconductor materials that are used in both linear and nonlinear all-optical integrated devices. Its excellent dielectric properties, high material stability, and dispersion controllability are attractive to on-chip optical communications, optical signal processing, and even imaging devices. However, a large-aperture SiN metasurface with high numerical aperture (NA) is limited by the low refractive index and nanofabrication technologies, particularly in the visible spectrum. Here, we experimentally realize the visible-spectrum SiN divergent metasurfaces by fabricating the 695-nm-thick hexagonal arrays with a minimum space of 42 nm between adjacent nanopillars. A micro-size divergent metasurface with NA~0.98 and subwavelength resolution enables objects to be shrunk as small as a single-mode fiber core. Another centimeter-size SiN divergent metasurface with over half a billion nanopillars, made by using the mature CMOS-compatible fabrication process, exhibits high-quality wide-angle imaging. Our findings may open a new door for the miniaturization of optical lenses in the fields of optical fibers, microendoscopes, and smart phones, as well as the applications in all-sky telescopes, large-angle beam shaping, and near-eye imaging.

DOI: 10.1103/PhysRevApplied.10.014005

I. INTRODUCTION

Over the last few years, metasurfaces have shown great potential to replace bulky optical components by virtue of their ultrathin and planar features [1–6]. By arranging the array of nanopillars properly, metasurfaces can almost realize arbitrary modulation on amplitude, phase, and/or polarization pixel-by-pixel on a subwavelength scale. Plenty of planar-device applications based on metasurfaces are possible; for example, beam-bending generators [7–9], holograms [10–16], wave plates [17–20], vortex beam generators [7,21–23], Bessel beam generators [24,25], and vector beam generators [26], etc. It is particularly practicable to design metasurfaces as arbitrary metasurfaces [24,27–47]. Considerable efforts have been made on these fantastic highly integrated metasurfaces, most of which were designed at the microwave [27,28] and near-infrared [24,29–37] regions. For instance, as reported in Ref. [30], a metasurface with high transmission

and focusing efficiency at some particular near-infrared wavelengths was fabricated using high-contrast dielectric nanopillars and high-precision nanofabrication technology, without the early use of lossy metallic materials [24,38–42]. Very recently, there has been a crucial development whereby metasurfaces have been designed and fabricated by low-contrast dielectric materials [22,43–48], resulting in many applications with visible-frequency and high-efficiency metasurfaces. Among low-contrast dielectric materials, silicon nitride (SiN) has been recognized as a fully CMOS-compatible platform for photonic devices at various wavelengths including the visible, telecommunication, and mid-infrared regions [49]. With a linear refractive index higher than that of silica, SiN can provide strong optical confinement in small waveguide dimensions, and does not suffer from two-photon absorption and the concomitant free-carrier absorption at communications wavelengths by virtue of its larger bandgap (~ 5 eV) than silicon (Si). Furthermore, the nonlinear refractive index of SiN is about an order of magnitude greater than silica. By controlling the thickness, the waveguide dispersion can be tailored to achieve phase matching and high mode confinement.

*chenyj69@mail.sysu.edu.cn

†dongjwen@mail.sysu.edu.cn

Numerical aperture (NA), a vital dimensionless measure of an optical lens system, is used to characterize the range of angles over which the system can accept or emit light, and impacts the light-gathering ability and imaging resolution ($\lambda/2\text{NA}$). A lens with a larger numerical aperture will have much better image performance on fine detail, brighter images, and a shallower depth of field. Numerous efforts are now being made to develop a high-NA metasurface [30,43–45]. A titanium dioxide metasurface with $\text{NA} \approx 0.8$ has been employed to achieve high-precision resolving power [43]. Most of the aforementioned metasurfaces have been designed as convergent lenses, yet in imaging systems, divergent lenses [41,42] are also important by virtue of their various functions on aberration correction. For example, a conventional doublet lens is made of a concave and a convex lens that match with each other. For wide-angle lens systems such as fish-eye and telephoto lenses, the divergent lens usually has much larger size and heavier weight than the convergent one. Therefore it is efficient to lighten the whole lens system with the miniaturization of the divergent lens.

In this work, we design polarization-insensitive divergent metasurfaces on the SiN platform. A 100- μm -diameter divergent metasurface with $\text{NA} \sim 0.98$ is fabricated on a 695-nm-thick SiN film. High resolving power and high transmission of 0.8 are observed near the wavelength of 633 nm. It can reduce objects as small as the core of single-mode fiber. Furthermore, a centimeter-size metasurface with over half a billion nanopillars has also been achieved by the mature CMOS-compatible fabrication process, showing great potential for wide-viewing-angle applications in macroscopic imaging system.

II. SIMULATION RESULTS OF PERIODIC GRATINGS

We first design a set of nanopillars with high transmittance and full 2π phase coverage in the periodic grating. Various kinds of dielectric nanopillars can be considered for metasurfaces, including slit [25,32], cuboid [43], cylinder [44], square cylinder [46], elliptic cylinder [35], and combined meta-molecules [31,34], etc. Such nanopillars can be divided into two types depending on their sensitivity to polarization. The polarization-sensitive nanopillars are spatial anisotropic and have rotation angles based on the theory of Pancharatnam-Berry phase, while polarization-insensitive ones are always cylinders or square cylinders, using diameters or side lengths to map the phases. Here, we choose cylindrical nanopillars to control the unpolarized light. Rectangular and hexagonal samples are also considered to discretize the continuous phase profile in the metasurface. Since the scattering of each nanopillar is a local effect and the coupling among nanopillars is weak, the difference in complex transmission coefficients between these

two sample methods are negligible [30]. However, hexagonal sampling can extend the limitation of the sampling interval and requires 13.4% fewer samples than rectangular sampling to reconstruct the circularly continuous bandlimited phase profile [50]. This means that it might be possible to reduce the burden of fabrication, especially for macro metasurfaces.

Figure 1(a) illustrates the schematic of the hexagonal SiN grating with a subwavelength lattice constant ($a = 416$ nm). As nanopillars stand on the silicon dioxide substrate, the lattice constant is less than the working wavelength of 633 nm in the substrate ($633 \text{ nm}/n_{\text{SiO}_2} = 436 \text{ nm}$) but greater than the diffraction condition ($633 \text{ nm}/2n_{\text{SiO}_2} = 218 \text{ nm}$). So there exists only zeroth-order diffraction for normal incidence, but it appears there is only feeble first-order diffraction for the oblique incidence case [51,52]. Rigorous coupled-wave analysis [53] is used to simulate the gratings. A y -polarized plane wave is normally incident on the SiN nanopillars from the substrate, yielding the complex transmission coefficient t and reflection coefficient r . The refractive index of SiN in the visible spectrum is approximately equal to 2. The maximum exiting phase is given by $\varphi_{\max} = 2\pi(n-1)d/\lambda$, where d is the thickness of a homogeneous film. To achieve a full 2π coverage, we set the thickness to be 695 nm, greater than the working wavelength of 633 nm. The transmission is polarization insensitive for normal incidence due to the geometric symmetry of the nanopillars. The focused magnetic field inside the nanopillars [white dashed lines in Fig. 1(b)] implies weak coupling in between them; it is the fundamental assumption of the metasurface design.

In order to give a complete picture to compare different dielectric materials, a parameter sweep of the complex transmission coefficient in the plane of nanopillar diameter and refractive index is shown in Figs. 1(c) and 1(d). In such cases, a lower refractive index (e.g. $n \approx 2$, the white vertical dashed lines) can support high and smooth transmission spectra within a broad diameter range from 50 to 400 nm, except for the low-transmission resonant dip at the diameter of 292 nm. The blue curve in Fig. 1(g) shows the corresponding transmission in the case of $n \approx 2$ and the red curve indicates the full 2π phase coverage. In contrast, there is a region of multiple resonances and poor transmission when the refractive index is large [upper-right of Fig. 1(c)]. In addition, a much lower refractive index cannot support the full 2π phase coverage, as illustrated in Fig. 1(d). As a result, one can just choose the material of SiN ($n \approx 2$) to achieve a full 2π phase coverage while maintaining high transmission at 633 nm.

Figures 1(e) and 1(f) show spectral responses of the SiN gratings. The transmission reaches close to one for a wide range from 530 to 780 nm except a few resonant dips [Fig. 1(e)]. However, a low transmission area can still be observed below 530 nm [blue curve in Fig. 1(h)], which

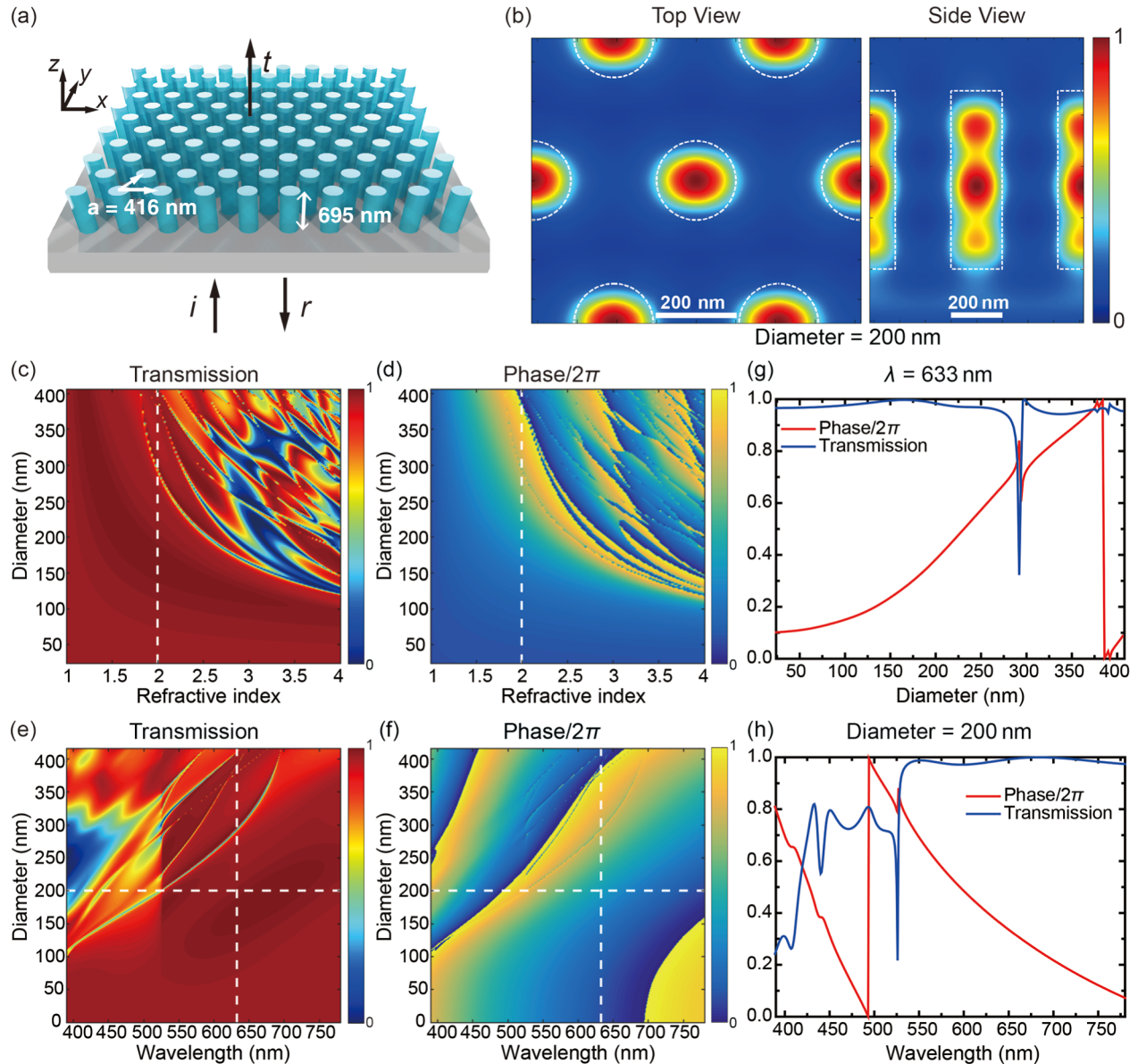


FIG. 1. Simulation results of SiN periodic gratings. (a) Schematic of the grating constructed by a low-refractive-index SiN array with circular nanopillars on a fused silica substrate. The hexagonal lattice constant is $a = 416 \text{ nm}$, and the thickness of nanopillars is 695 nm. (b) Top and side views of the normalized magnetic field intensity at the nanopillar diameter of 200 nm. The white dashed frame depicts the boundaries of the SiN nanopillars. A plane wave with y polarization is normally incident onto the SiN nanopillars from the bottom of the substrate. Scale bar, 200 nm. (c),(d) Calculated transmission and its phase as a function of the refractive index and the post diameter at $\lambda = 633 \text{ nm}$. (e),(f) Calculated transmission and its phase as a function of the wavelength and the post diameter with refractive index $n = 2$. (g) The profile of the vertical dashed lines in panels (c)–(f), showing the full 2π phase coverage and the close-to-one transmission spectrum for a family of SiN periodic gratings at $\lambda = 633 \text{ nm}$. (h) The profile of the horizontal dashed lines in panels (e) and (f), illustrating the spectral response for SiN periodic gratings with the nanopillar diameter of 200 nm and the high efficiency in broadband visible region.

should be avoided when choosing the discrete nanopillars in the subsequent round of design. Figure 1(e) displays the full 2π phase coverage in the visible spectrum. More than 2π phase coverage in the lower-wavelength area implies great flexibility of SiN for designing at lower wavelengths. Though a low transmission area also exists

in the lower-wavelength area as shown in Fig. 1(e), it can be removed by properly adjusting the thickness of nanopillars. In brief, the proposed SiN nanopillar parameters can support high transmission in the broadband visible region and provide the full 2π phase coverage in the designed wavelength, enabling an arbitrary transmission

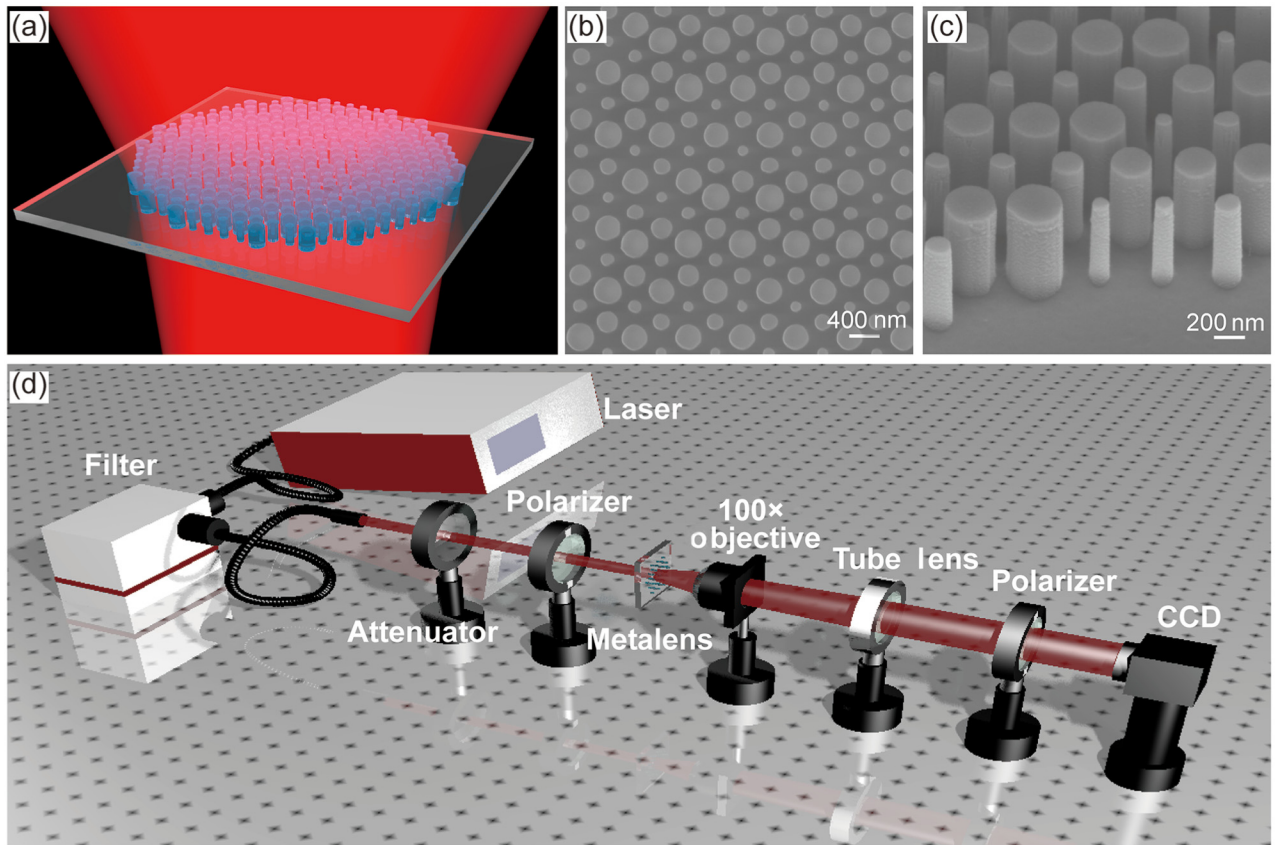


FIG. 2. Schematic diagram, SEM images and measurement setup of the 100- μm -diameter micro metalens. (a) Schematic diagram of a divergent metalens operating in the transmission mode. (b) Top-view SEM image of a portion of the fabricated micro metalens. Scale bar, 400 nm. (c) Side-view SEM image with high magnification. Scale bar, 200 nm. (d) Measurement setup for characterizing the chromatic dispersion features of the micro metalens.

phase profile by appropriately arranging the nanopillars in a nonresonant regime.

III. DESIGN OF CLOSE-TO-ONE NA METALENS

We choose the spatial phase profile of the metalens as a divergent lens, illustrated in Fig. 2(a). The divergent phase profile can be expressed by

$$\phi(x, y) = \frac{2\pi}{\lambda} (\sqrt{x^2 + y^2 + f^2} - |f|),$$

where $\lambda = 633$ nm is the designed wavelength, f is the focal length, and (x, y) is the in-plane coordinate of each point in the phase profile. We discretize the continuous divergent phase profile onto a hexagonal lattice with the subwavelength lattice constant, and then place six types of nanopillars on the silicon dioxide substrate in discrete positions. The diameters of the selected nanopillars vary from 170 to 374 nm, mapping six linear orders between 0 and 2π [cf. Fig. 1(g)] and keeping high transmission [cf. Fig. 1(e)]. It yields a maximum aspect ratio of $\sim 1:4$ and a minimum space of 42 nm between adjacent nanopillars. In the

first design, the micro metalens has a diameter of 100 μm and a focal length of $-10 \mu\text{m}$. The NA of the metalens is as large as 0.98. It follows that the narrowest width of the outermost region is close to wavelength scale ($\sim \lambda/\text{NA}$) and the quantized number is not six, impairing the metalens performance.

In order to evaluate the performance of the designed metalens, we propose two simple and quick methods based on the fundamental assumption of independent response among nanopillars: the ideal-post method and the grating-cell method (see Supplemental Material, Sec. IV [54]). As shown in Fig. S3, both results conform to that in the finite-difference time-domain (FDTD) method. All of the results support only one virtual focus in the designed focal length, verifying the design feasibility of our metalens. With these anticipated evaluation results, we carry on the next challenging fabrication process (see [55,56] and Supplemental Material, Sec. I [54]). Scanning electron microscope (SEM) images of the 100- μm -diameter micro metalens are exhibited. The top-view SEM image of a portion of the fabricated micro metalens with high magnification is displayed in Fig. 2(b). The side-view SEM

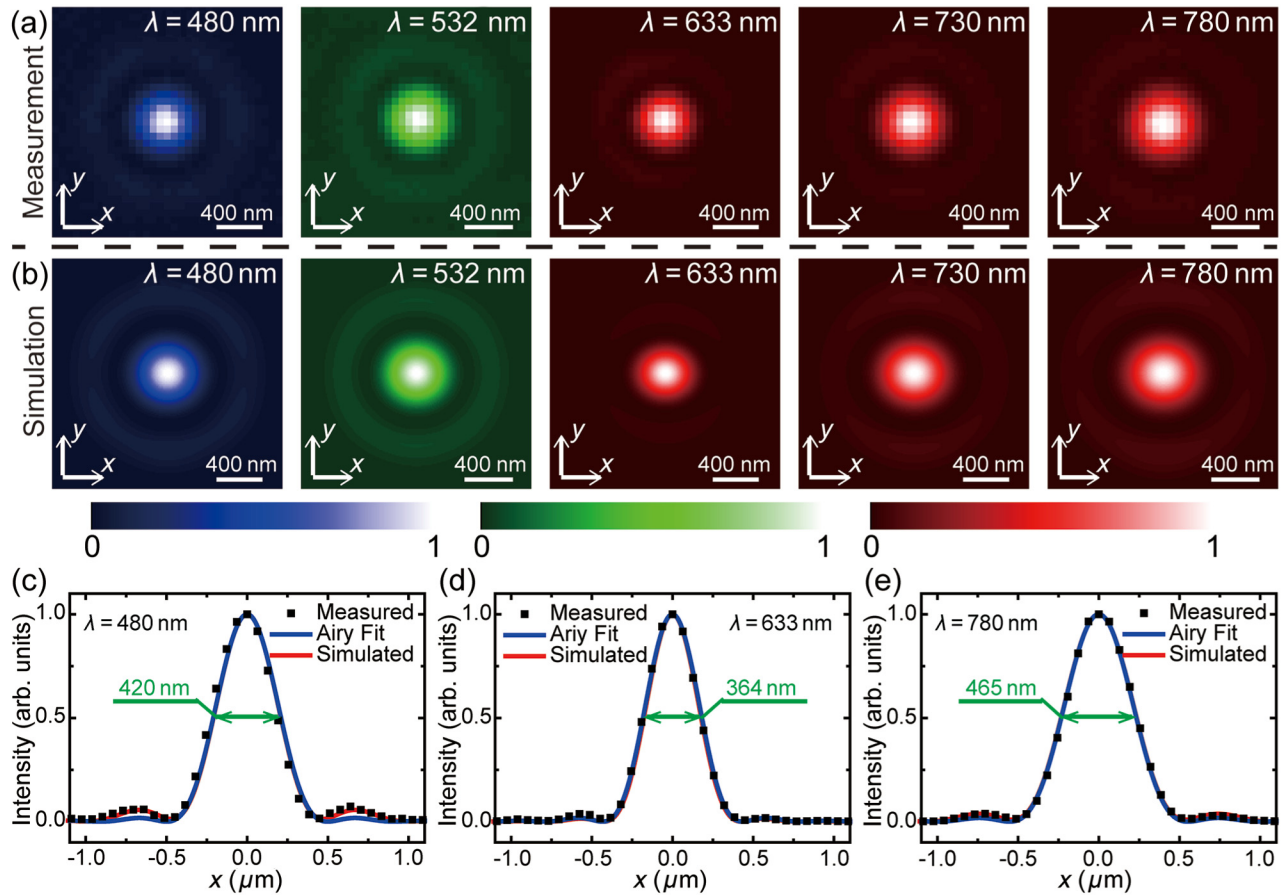


FIG. 3. The virtual focal planes of the micro metalens. (a),(b) Measurement and simulation of intensity patterns in the virtual focal planes at five different wavelengths of 480, 532, 633, 730, and 780 nm. Three kinds of pseudocolors are used for color bars. Scale bar, 400 nm. (c)–(e) The x -direction cross sections of the measured and simulated intensity profiles at three wavelengths. The red solid curve denotes the simulated results while the blue solid curve is Airy fit of measured data (black square point). The green text gives the full widths at half-maximums (FWHMs) of the fitting measured data, showing the subwavelength virtual focus spots.

image in Fig. 2(c) describes the vertical profile of the nanopillars.

IV. CHARACTERIZATIONS OF DIVERGENT MICRO METALENS

We have a virtual focal spot due to the negative focal length of the divergent micro lens. To characterize such virtual focal spot, we measure the focusing effect at different wavelengths from 480 to 780 nm in the visible spectrum. The measurement setup is illustrated in Fig. 2(d) and more details can be found in Supplemental Material, Sec. I [54]. Figure 3(a) shows the intensity profile in the virtual focal planes of five discrete wavelengths, depicted by pseudocolors. One can find that the intensity is highly confined at the center and the spot size is at subwavelength scale, enabling broadband imaging with high resolution. The simulation results calculated by field-tracing method [57] are consistent with the measurements shown in Fig. 3(a), even for the feeble side lobes around the center spots.

To evaluate the center spot quantitatively, we plot out the cross sections of the spot for all five wavelengths, and illustrate the intensity profiles in the x direction at 480, 633, and 780 nm in Figs. 3(c)–3(e). The remaining results are gathered in Fig. S6. The red (blue) curves represent the simulation (Airy fits) results while the dots denote the measurement data. A prominent feature is the ability to gain a subwavelength-size virtual focus spot at 633 nm, by verifying the value of the full width at half-maximum (FWHM) to be 364 nm, very close to the simulation value of 357 nm. The subwavelength spots are also found in other wavelengths of 480, 532, 730, and 780 nm, with the differences between measurement and simulation of less than 4.5%. Note that the FWHM values do not increase monotonously from the blue to the red region and it reaches the minimum at the designed wavelength of 633 nm, deviating from that of traditional diffraction microelements and leading to some unexpected chromatic aberration in optical imaging. Figure S7 shows that the modulation transfer function (MTF) drops with the large cutoff spatial frequency of

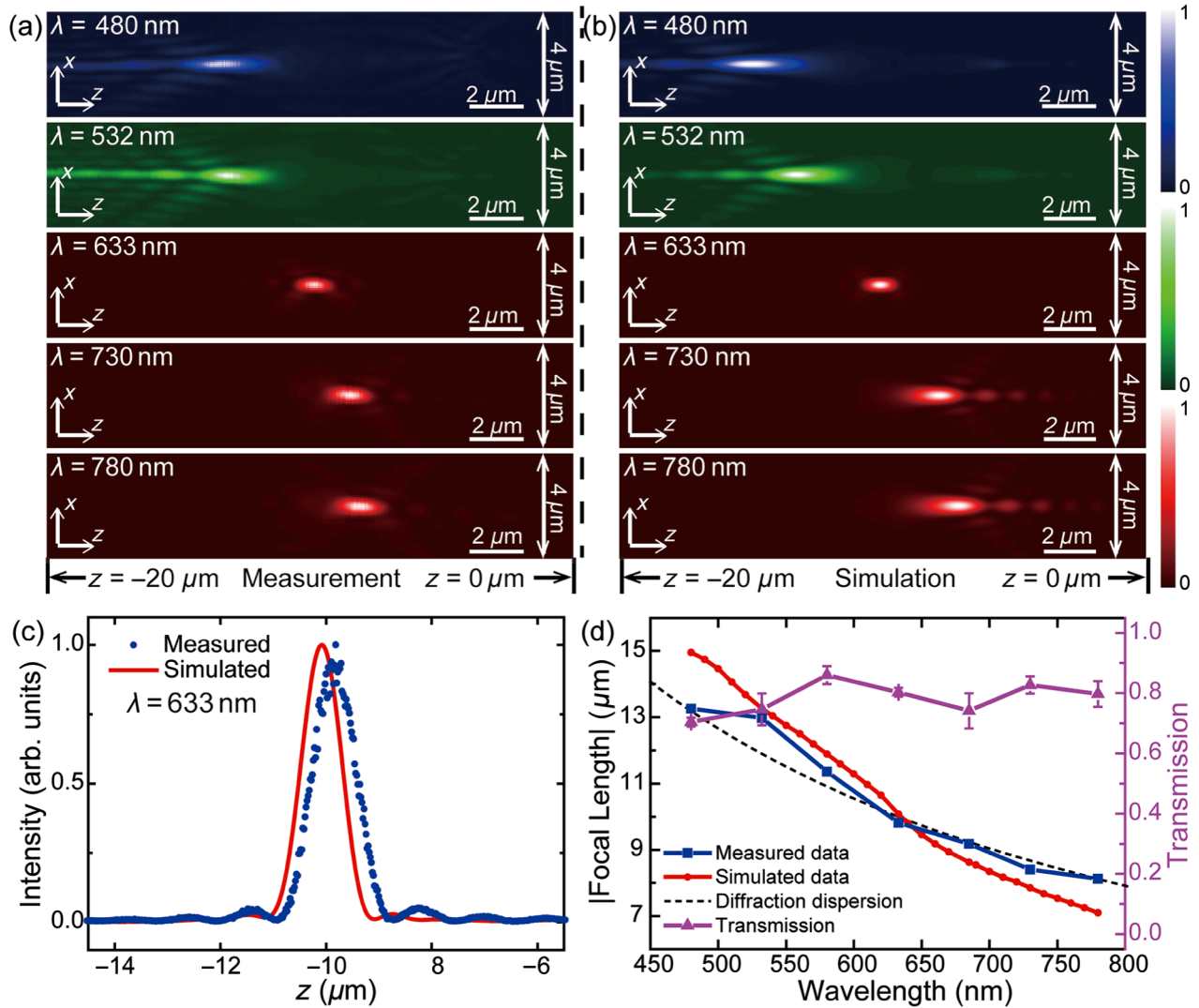


FIG. 4. The x - z planes of the micro metalens in different wavelengths. (a),(b) Normalized measured and simulated intensity distributions in x - z planes at different wavelengths. Three kinds of pseudocolors are used for color bars. Scale bar, $2 \mu\text{m}$. (c) The z -direction cross sections at 633 nm . The red solid curve is the simulated data and the blue points are measured data, showing no significant difference with simulated data except for a little deviation of focus point. (d) Measured and simulated virtual focal lengths of the micro metalens as a function of wavelength. The black dashed curve represents the dispersion of diffraction optical element with an expression of $f = \lambda_{\text{center}} \times f_{\text{center}}/\lambda$, where the subscript stands for the center wavelength. It notes that the chromatic dispersion of the metalens is mainly due to the diffraction dispersion. The pink curve demonstrates the measured transmission spectrum, which comes up to as high as $\sim 80\%$. The error bars represent the standard deviation for three measurement repetitions.

about 2500 cyc/mm, indicating high resolution at different wavelengths. Here, the MTF is obtained by the modulus of the discrete Fourier transform of the measured intensity distribution in the x and y directions in Fig. 3(a).

Figure 4 depicts the focal spots of the divergent metalens along the propagation z direction at five different wavelengths. The focal spots locate within the negative- z position while the metalens is placed on the plane of $z = 0$. It is clearly seen from the consistent results between measurements and simulations in Figs. 4(a) and 4(b), verifying the diverging feature of the metalens. At the center wavelength of 633 nm , e.g. the third row in Figs. 4(a) and

4(b), there is the remarkable feature that only one focal spot is observed at the distance of $-10 \mu\text{m}$. This is strong evidence for the realization of air NA with the value as large as 0.98. The measured focal spot has little position deviation from the simulation [Fig. 4(c)], but it will have no impact on the lateral imaging quality. For other wavelengths beyond 633 nm , several secondary focal points exist along the propagation direction, locating at different distances from the metalens. In particular, such secondary focal points of shorter wavelengths are further away from the metalens than those of longer ones. It leads to a slender tail around the main focal point, bringing additional

monochromatic aberrations for imaging and adverse influence on the device.

Figure 4(d) illustrates that the focal length decreases from blue to red wavelengths, with the same tendency as the conventional diffraction dispersion of binary optics. But such chromatic dispersion in the metalens is a little more serious compared to the conventional binary optics with an expression of $f = \lambda_{\text{center}} \times f_{\text{center}}/\lambda$, where the subscript stands for the center wavelength. Both measured (blue) and simulated (red) curves have larger slopes than the conventional case (dashed). Note that there is also a slight difference between measurement and simulation except for the center wavelength. The chromatic dispersion in the metalens arises mainly from the phase-wrapping discontinuities and can be corrected by proper methods to achieve full-color imaging [58–60]. The transmission spectrum is also measured by a homemade transmission setup (Fig. S4), and it comes up to as high as $\sim 80\%$ in the visible spectrum, manifesting the advantage of high transparency through the SiN material.

V. IMAGE DEMONSTRATIONS OF METALENSSES

In order to demonstrate the capability for practical imaging, we employ the above divergent metalens to image a logo “SYSU” with the actual physical size of $300 \times 340 \mu\text{m}^2$. The measurement configuration schematic is drawn in Fig. 5(a). A white light source (Thorlabs OSL2) is applied to illuminate the logo SYSU through a pinhole. A series of narrow-band (10 nm) filters (not shown in the light path) with different center wavelengths are placed between the lamp and the pinhole. An attenuator is utilized to control the intensity of the incident light. To conveniently adjust the relative distance between the object and the metalens, a $40\times$ objective (GCO-21) is used to gather the rays from the logo, so as to obtain the first size-reduced logo image as the object of the metalens. This object is then secondly imaged by the divergent metalens to form a more reduced virtual image, and finally observed by a microscopy system consisting of a $100\times$ objective (Olympus MPLFLN100xBD), a tube lens (Thorlabs ITL200), and a color charge-coupled device (CCD) camera (Mshot MC20). Figure 5(b) plots out the schematic diagram in a much simpler format. The logo and the $40\times$ objective are mounted on the same multi-axis translation stages. Once the distance between the logo and the $40\times$ objective is determined, they will be moved together to ensure that the object will not change except for its position.

One can see in Fig. 5(c) that the object with the size of $\sim 23 \times 28 \mu\text{m}^2$ is the reduced image of the original logo SYSU through the $40\times$ objective at the wavelength of 635 nm. After inserting the divergent metalens, a more reduced virtual image is captured by the microscopy system. In the measurement, the final virtual image has a size of $\sim 3 \times 3.6 \mu\text{m}^2$, shrinking to about 1/59 of the object

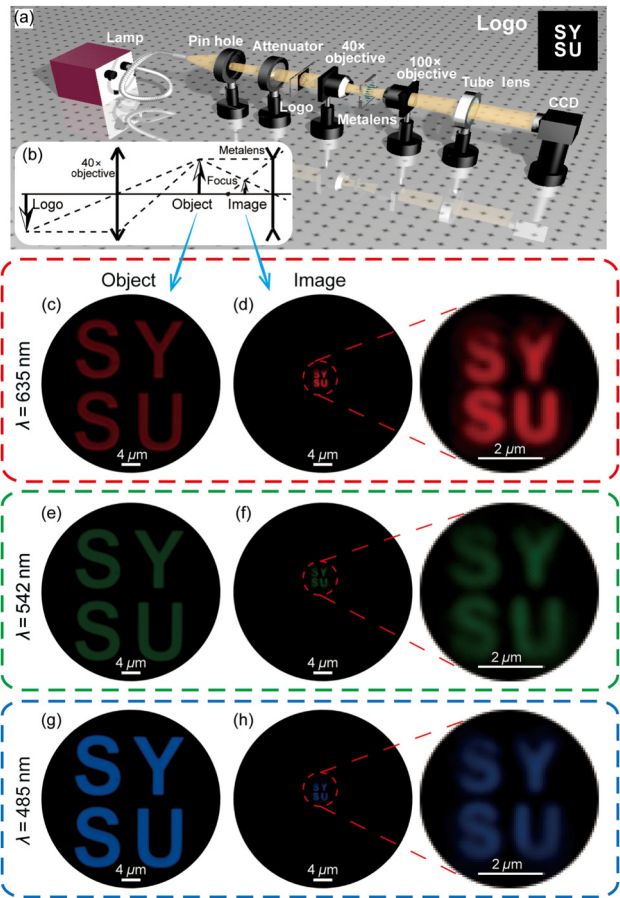


FIG. 5. Image demonstrations of the micro metalens. (a) Measurement configuration for image demonstrations of the micro metalens. (b) A simple schematic diagram of the imaging mechanism among the logo, the $40\times$ objective, and the micro metalens. (c) The object illuminated by inserting narrow-band (10 nm) filters of 635 nm between the lamp and pinhole. Scale bar, $4 \mu\text{m}$. (d) The corresponding image of (c) observed by the micro metalens and its enlarged view of the red dashed circular area. The whole object has been reduced to the small circular field-of-view, implying a wide field-of-view potential for imaging. (e)–(h) The corresponding results at wavelengths of 485 and 542 nm.

size. The whole object is reduced to the ultra-small circular field-of-view highlighted by the red dashed circle in Fig. 5(d), implying a potential application of wide field-of-view imaging. However, strong shrinking ability will somehow degrade imaging resolution due to monochromatic aberrations. For example, the boundaries of the letters SYSU become blurred after metalens reduction, compared with the much sharper boundary without the metalens. The imaging degradation may come from several aspects. First is the sample rate, which is not high enough for the close-to-one NA value. The undersampling causes the mismatch between the discrete spatial phase profile and the continuous one. Second is the responses of nanopillars in the metalens being somewhat inconsistent with those in the

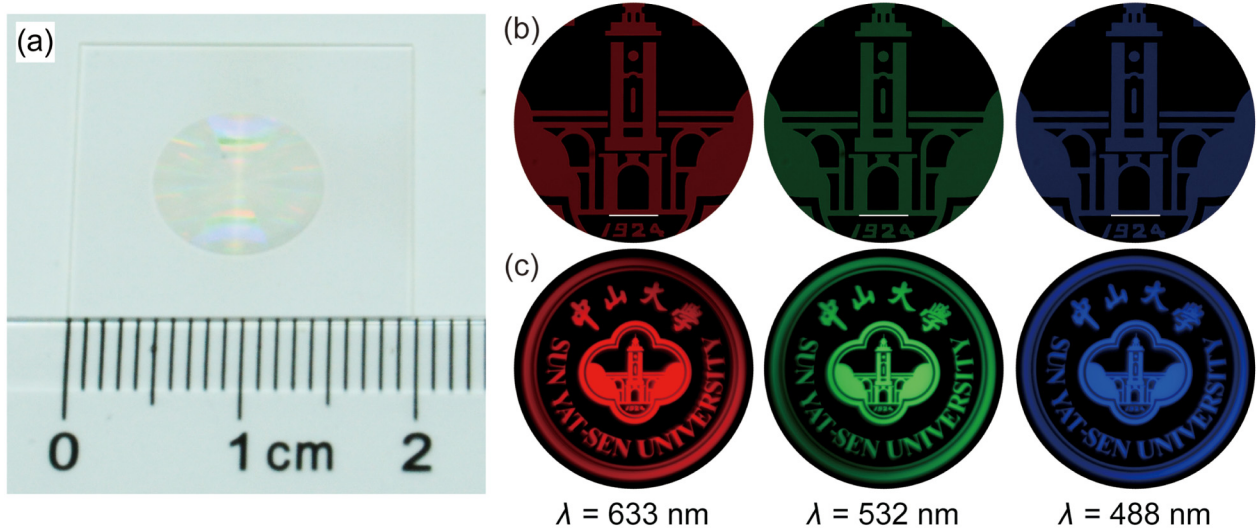


FIG. 6. Image demonstrations of the macro metalens. (a) Photograph of the macroscopic metalens with a focal length of -4 mm, in which the ruler is used to emphasize its 1-cm-diameter size. The number of nanopillars in such macroscopic metalens is over half a billion. (b) The central parts of object logos observed by the $10\times$ objective without the macroscopic metalens at three different wavelengths, respectively. Scale bar, $100\ \mu\text{m}$. (c) The entire logo in the same areas of (b) on the CCD camera, showing the wider field of view.

periodic grating, leading to the distortion of the spatial frequency spectrum. In addition, fabrication defects and measurement error may also increase the aberrations. In other words, one may obtain an ultra-wide field of view from the high NA divergent metalens, but it will lose some details of the object.

Figures 5(e)–5(h) show the images at 485 and 542 nm, respectively. These results are similar to those at 635 nm. All letters in both images can still be clearly recognized, showing the high resolution at these wavelengths. Note that the final image can be reduced to a size of about $3 \times 3.6\ \mu\text{m}^2$, very close to the size of a piece of single-mode optical fiber. This means that if the metalens would mount on the fiber end face, one might use such metafiber to image objects with a wide field of view so that more information can be gained than before. Furthermore, as the spatial phase profile of the metalens can be designed arbitrarily, it may inspire an interesting idea to design a metalens with multiple focal points [37] in the same focal plane, which might provide another alternative for the applications of array imaging.

Based on the above considerations, we further fabricate a macroscopic metalens with a diameter of 1 cm and a focal length of -4 mm, yielding a little lower NA ≈ 0.78 . Note that the number of nanopillars in the 1-cm-diameter macroscopic metalens is over half a billion, which means that it needs to consume large resources (including preparation time and equipment) to fabricate. The 1-cm-diameter metalens is manufactured by electron-beam lithography. During the process, a larger electron-beam size and faster electron-beam current were carefully chosen to expose the pattern, in order to reduce the exposure time to an

acceptable 6 h. Figure 6(a) shows the photograph of the actual sample in which the ruler is used to emphasize the 1-cm-diameter metalens. To display its wide field-of-view application, we first use the macroscopic metalens to directly observe a logo using the measurement setup in Fig. S5. Figures 6(b) and 6(c), show the original objects without and with the macroscopic metalens, respectively. It is clear that in the same circular area of the CCD camera, one can have much more field of view in Fig. 6(c) than those in Fig. 6(b), indicating that the macroscopic metalens broadens the system horizon.

VI. DISCUSSION

In conclusion, we demonstrate the low-contrast dielectric metasurface as a divergent metalens with close-to-one NA. High transmission is achieved for unpolarized visible light by using the hexagonal array of cylindrical nanopillars based on the SiN platform. We fabricate the close-to-one NA metalens with $100\ \mu\text{m}$ diameter and 695-nm-thick SiN nanopillar array, which has a maximum aspect ratio $\sim 1:4$ and a minimum space of 42 nm between adjacent nanopillars. The quick simulation method of field tracing is proposed to evaluate the metalens. The experimental results are very consistent with the designs, showing the unique virtual focal spot with the subwavelength FWHM and high resolving power. The macroscopic high-NA metalens with 1 cm diameter, which consists of over half billion nanopillars, is also fabricated. Each metalens is capable of wide field-of-view imaging.

It is expected that the divergent metalens can be used for integration in microscopic optical systems like optical

fibers and the miniaturization of endoscopes. Moreover, it could be applied to macroscopic optical devices like smartphones and telescopes by fabricating metaspheres with a much larger aperture. With CMOS compatibility of SiN materials and its superiority in nonlinear optics, it may inspire future work to integrate metaspheres into optoelectronic devices, e.g. on-chip optical interconnections.

ACKNOWLEDGMENTS

This work was supported by National Basic Research Program of China (973 Program) (Grant No. 2014CB340000), National Natural Science Foundation of China (Grants No. 11522437, 61775243, 61323001, 61490715, 11690031, 51403244, 11774437, U1701661), Science and Technology Program of Guangzhou (Grants No. 201707020017, 201804020029), Natural Science Foundation of Guangdong Province (Grant No. 2017A030310510), Local Innovative and Research Teams Project of Guangdong Pearl River Talents Program (Grant No. 2017BT01X121). Z.-B.F. and Z.-K.S. contributed equally to this work.

- [1] A. V. Kildishev, A. Boltasseva, and V. M. Shalaev, Planar photonics with metasurfaces, *Science* **339**, 1232009 (2013).
- [2] N. Yu and F. Capasso, Flat optics with designer metasurfaces, *Nat. Mater.* **13**, 139 (2014).
- [3] A. M. Shaltout, A. V. Kildishev, and V. M. Shalaev, Evolution of photonic metasurfaces: From static to dynamic, *J. Opt. Soc. Am. B* **33**, 501 (2016).
- [4] C. Hou-Tong, J. T. Antoinette, and Y. Nanfang, A review of metasurfaces: Physics and applications, *Rep. Prog. Phys.* **79**, 076401 (2016).
- [5] S. Jahani and Z. Jacob, All-dielectric metamaterials, *Nat. Nanotechnol.* **11**, 23 (2016).
- [6] L. Zhang, S. Mei, K. Huang, and C.-W. Qiu, Advances in full control of electromagnetic waves with metasurfaces, *Adv. Opt. Mater.* **4**, 818 (2016).
- [7] N. Yu, P. Genevet, M. A. Kats, F. Aieta, J.-P. Tetienne, F. Capasso, and Z. Gaburro, Light propagation with phase discontinuities: Generalized laws of reflection and refraction, *Science* **334**, 333 (2011).
- [8] X. Ni, N. K. Emani, A. V. Kildishev, A. Boltasseva, and V. M. Shalaev, Broadband light bending with plasmonic nanoantennas, *Science* **335**, 427 (2012).
- [9] Z. Zhou, J. Li, R. Su, B. Yao, H. Fang, K. Li, L. Zhou, J. Liu, D. Stellinga, C. P. Reardon, T. F. Krauss, and X. Wang, Efficient silicon metasurfaces for visible light, *ACS Photon.* **4**, 544 (2017).
- [10] W. T. Chen, K.-Y. Yang, C.-M. Wang, Y.-W. Huang, G. Sun, I. D. Chiang, C. Y. Liao, W.-L. Hsu, H. T. Lin, S. Sun, L. Zhou, A. Q. Liu, and D. P. Tsai, High-efficiency broadband meta-hologram with polarization-controlled dual images, *Nano Lett.* **14**, 225 (2014).
- [11] X. Ni, A. V. Kildishev, and V. M. Shalaev, Metasurface holograms for visible light, *Nat. Commun.* **4**, 2807 (2013).
- [12] D. Wen, F. Yue, G. Li, G. Zheng, K. Chan, S. Chen, M. Chen, K. F. Li, P. W. H. Wong, K. W. Cheah, E. Yue Bun Pun, S. Zhang, and X. Chen, Helicity multiplexed broadband metasurface holograms, *Nat. Commun.* **6**, 8241 (2015).
- [13] G. Zheng, H. Mühlenbernd, M. Kenney, G. Li, T. Zentgraf, and S. Zhang, Metasurface holograms reaching 80% efficiency, *Nat. Nanotechnol.* **10**, 308 (2015).
- [14] B. Wang, F. Dong, Q.-T. Li, D. Yang, C. Sun, J. Chen, Z. Song, L. Xu, W. Chu, Y.-F. Xiao, Q. Gong, and Y. Li, Visible-frequency dielectric metasurfaces for multiwavelength achromatic and highly dispersive holograms, *Nano Lett.* **16**, 5235 (2016).
- [15] L. Li, T. Jun Cui, W. Ji, S. Liu, J. Ding, X. Wan, Y. Bo Li, M. Jiang, C.-W. Qiu, and S. Zhang, Electromagnetic reprogrammable coding-metasurface holograms, *Nat. Commun.* **8**, 197 (2017).
- [16] F. Walter, G. Li, C. Meier, S. Zhang, and T. Zentgraf, Ultrathin nonlinear metasurface for optical image encoding, *Nano Lett.* **17**, 3171 (2017).
- [17] Y. Zhao and A. Alù, Manipulating light polarization with ultrathin plasmonic metasurfaces, *Phys. Rev. B* **84**, 205428 (2011).
- [18] N. Yu, F. Aieta, P. Genevet, M. A. Kats, Z. Gaburro, and F. Capasso, A Broadband, Background-free quarter-wave plate based on plasmonic metasurfaces, *Nano Lett.* **12**, 6328 (2012).
- [19] Y. Zhao and A. Alù, Tailoring the dispersion of plasmonic nanorods to realize broadband optical meta-waveplates, *Nano Lett.* **13**, 1086 (2013).
- [20] F. Ding, Z. Wang, S. He, V. M. Shalaev, and A. V. Kildishev, Broadband high-efficiency half-wave plate: A supercell-based plasmonic metasurface approach, *ACS Nano* **9**, 4111 (2015).
- [21] Y. Yang, W. Wang, P. Moitra, I. I. Kravchenko, D. P. Briggs, and J. Valentine, Dielectric meta-reflectarray for broadband linear polarization conversion and optical vortex generation, *Nano Lett.* **14**, 1394 (2014).
- [22] A. Zhan, S. Colburn, R. Trivedi, T. K. Fryett, C. M. Dodson, and A. Majumdar, Low-contrast dielectric metasurface optics, *ACS Photon.* **3**, 209 (2016).
- [23] M. Q. Mehmood, S. Mei, S. Hussain, K. Huang, S. Y. Siew, L. Zhang, T. Zhang, X. Ling, H. Liu, J. Teng, A. Danner, S. Zhang, and C.-W. Qiu, Visible-frequency metasurface for structuring and spatially multiplexing optical vortices, *Adv. Mater.* **28**, 2533 (2016).
- [24] F. Aieta, P. Genevet, M. A. Kats, N. Yu, R. Blanchard, Z. Gaburro, and F. Capasso, Aberration-free ultrathin flat lenses and axicons at telecom wavelengths based on plasmonic metasurfaces, *Nano Lett.* **12**, 4932 (2012).
- [25] D. Lin, P. Fan, E. Hasman, and M. L. Brongersma, Dielectric gradient metasurface optical elements, *Science* **345**, 298 (2014).
- [26] H. Chen, Z. Chen, Q. Li, H. Lv, Q. Yu, and X. Yi, Generation of vector beams based on dielectric metasurfaces, *J. Mod. Optic.* **62**, 638 (2015).
- [27] H.-X. Xu, S. Ma, W. Luo, T. Cai, S. Sun, Q. He, and L. Zhou, Aberration-free and functionality-switchable metasurfaces based on tunable metasurfaces, *Appl. Phys. Lett.* **109**, 193506 (2016).

- [28] K. Chen, Y. Feng, F. Monticone, J. Zhao, B. Zhu, T. Jiang, L. Zhang, Y. Kim, X. Ding, S. Zhang, A. Alù, and C.-W. Qiu, A reconfigurable active Huygens' metasens, *Adv. Mater.* **29**, 1606422 (2017).
- [29] P. R. West, J. L. Stewart, A. V. Kildishev, V. M. Shalaev, V. V. Shkunov, F. Strohkendl, Y. A. Zakharenkov, R. K. Dodds, and R. Byren, All-dielectric subwavelength metasurface focusing lens, *Opt. Express* **22**, 26212 (2014).
- [30] A. Arbabi, Y. Horie, A. J. Ball, M. Bagheri, and A. Faraon, Subwavelength-thick lenses with high numerical apertures and large efficiency based on high-contrast transmittarrays, *Nat. Commun.* **6**, 7069 (2015).
- [31] E. Arbabi, A. Arbabi, S. M. Kamali, Y. Horie, and A. Faraon, Multiwavelength polarization-insensitive lenses based on dielectric metasurfaces with meta-molecules, *Optica* **3**, 628 (2016).
- [32] M. Khorasaninejad, F. Aieta, P. Kanhaiya, M. A. Kats, P. Genevet, D. Rousso, and F. Capasso, Achromatic metasurface lens at telecommunication wavelengths, *Nano Lett.* **15**, 5358 (2015).
- [33] F. Aieta, M. A. Kats, P. Genevet, and F. Capasso, Multiwavelength achromatic metasurfaces by dispersive phase compensation, *Science* **347**, 1342 (2015).
- [34] S. Shrestha, A. Overvig, and N. Yu, in Conference on Lasers and Electro-Optics (Optical Society of America, San Jose, CA, 2017), p. FM1H.3.
- [35] E. Arbabi, A. Arbabi, S. M. Kamali, Y. Horie, and A. Faraon, High efficiency double-wavelength dielectric metasurface lenses with dichroic birefringent meta-atoms, *Opt. Express* **24**, 18468 (2016).
- [36] E. Arbabi, A. Arbabi, S. M. Kamali, Y. Horie, and A. Faraon, Controlling the sign of chromatic dispersion in diffractive optics with dielectric metasurfaces, *Optica* **4**, 625 (2017).
- [37] L. Rongzhen, S. Fei, S. Yongxuan, W. Wei, Z. Lie, and G. Zhongyi, Broadband, high-efficiency, arbitrary focusing lens by a holographic dielectric meta-reflectarray, *J. Phys. D Appl. Phys.* **49**, 145101 (2016).
- [38] L. Verslegers, P. B. Catrysse, Z. Yu, J. S. White, E. S. Barnard, M. L. Brongersma, and S. Fan, Planar lenses based on nanoscale slit arrays in a metallic film, *Nano Lett.* **9**, 235 (2009).
- [39] X. Chen, M. Chen, M. Q. Mehmood, D. Wen, F. Yue, C.-W. Qiu, and S. Zhang, Longitudinal multifoci metasens for circularly polarized light, *Adv. Opt. Mater.* **3**, 1201 (2015).
- [40] X. Ni, S. Ishii, A. V. Kildishev, and V. M. Shalaev, Ultra-thin, planar, Babinet-inverted plasmonic metasens, *Light Sci. Appl.* **2**, e72 (2013).
- [41] X. Chen, L. Huang, H. Mühlenbernd, G. Li, B. Bai, Q. Tan, G. Jin, C.-W. Qiu, S. Zhang, and T. Zentgraf, Dual-polarity plasmonic metasens for visible light, *Nat. Commun.* **3**, 1198 (2012).
- [42] X. Chen, L. Huang, H. Mühlenbernd, G. Li, B. Bai, Q. Tan, G. Jin, C.-W. Qiu, T. Zentgraf, and S. Zhang, Reversible three-dimensional focusing of visible light with ultrathin plasmonic flat lens, *Adv. Opt. Mater.* **1**, 517 (2013).
- [43] M. Khorasaninejad, W. T. Chen, R. C. Devlin, J. Oh, A. Y. Zhu, and F. Capasso, Metasens at visible wavelengths: Diffraction-limited focusing and subwavelength resolution imaging, *Science* **352**, 1190 (2016).
- [44] M. Khorasaninejad, A. Y. Zhu, C. Roques-Carmes, W. T. Chen, J. Oh, I. Mishra, R. C. Devlin, and F. Capasso, Polarization-insensitive metasens at visible wavelengths, *Nano Lett.* **16**, 7229 (2016).
- [45] W. T. Chen, A. Y. Zhu, M. Khorasaninejad, Z. Shi, V. Sanjeev, and F. Capasso, Immersion meta-lenses at visible wavelengths for nanoscale imaging, *Nano Lett.* **17**, 3188 (2017).
- [46] M. Khorasaninejad, Z. Shi, A. Y. Zhu, W. T. Chen, V. Sanjeev, A. Zaidi, and F. Capasso, Achromatic metasens over 60 nm bandwidth in the visible and metasens with reverse chromatic dispersion, *Nano Lett.* **17**, 1819 (2017).
- [47] B. Groever, W. T. Chen, and F. Capasso, Meta-lens doublet in the visible region, *Nano Lett.* **17**, 4902 (2017).
- [48] A. Zhan, S. Colburn, C. M. Dodson, and A. Majumdar, Metasurface freeform nanophotonics, *Sci. Rep.* **7**, 1673 (2017).
- [49] D. J. Moss, R. Morandotti, A. L. Gaeta, and M. Lipson, New CMOS-compatible platforms based on silicon nitride and Hydex for nonlinear optics, *Nat. Photon.* **7**, 597 (2013).
- [50] D. E. Dudgeon and R. M. Mersereau, *Multidimensional Digital Signal Processing* (Prentice Hall, New Jersey, 1990).
- [51] J. R. Marcante and D. H. Raguin, High-efficiency, high-dispersion diffraction gratings based on total internal reflection, *Opt. Lett.* **29**, 542 (2004).
- [52] E. B. Grann, M. G. Moharam, and D. A. Pommet, Optimal design for antireflective tapered two-dimensional subwavelength grating structures, *J. Opt. Soc. Am. A* **12**, 333 (1995).
- [53] V. Liu and S. Fan, S4 : A free electromagnetic solver for layered periodic structures, *Comput. Phys. Commun.* **183**, 2233 (2012).
- [54] See Supplemental Material at <http://link.aps.org/supplemental/10.1103/PhysRevApplied.10.014005> for additional information on the design and measurement of the metasens.
- [55] Z. Shao, Y. Chen, H. Chen, Y. Zhang, F. Zhang, J. Jian, Z. Fan, L. Liu, C. Yang, L. Zhou, and S. Yu, Ultra-low temperature silicon nitride photonic integration platform, *Opt. Express* **24**, 1865 (2016).
- [56] C. Yin, Y. Chen, X. Jiang, Y. Zhang, Z. Shao, P. Xu, and S. Yu, Realizing topological edge states in a silicon nitride microring-based photonic integrated circuit, *Opt. Lett.* **41**, 4791 (2016).
- [57] F. Wyrowski and M. Kuhn, Introduction to field tracing, *J. Mod. Optic.* **58**, 449 (2011).
- [58] W. T. Chen, A. Y. Zhu, V. Sanjeev, M. Khorasaninejad, Z. Shi, E. Lee, and F. Capasso, A broadband achromatic metasens for focusing and imaging in the visible, *Nat. Nanotechnol.* **13**, 220 (2018).
- [59] S. Colburn, A. Zhan, and A. Majumdar, Metasurface optics for full-color computational imaging, *Sci. Adv.* **4**, eaar2114 (2018).
- [60] S. Wang, P. C. Wu, V.-C. Su, Y.-C. Lai, M.-K. Chen, H. Y. Kuo, B. H. Chen, Y. H. Chen, T.-T. Huang, J.-H. Wang, R.-M. Lin, C.-H. Kuan, T. Li, Z. Wang, S. Zhu, and D. P. Tsai, A broadband achromatic metasens in the visible, *Nat. Nanotechnol.* **13**, 227 (2018).